UC Riverside
UC Riverside Previously Published Works

Title

Size-dependent piezoelectric and mechanical properties of electrospun P(VDF-TrFE) nanofibers for enhanced energy harvesting

Authors

Ico, G
Showalter, A
Bosze, W
et al.

Size-Dependent Piezoelectric and Mechanical Properties of Electrospun P(VDF-TrFE) Nanofibers for Enhanced Energy Harvesting

Gerardo Ico[1], Adam Showalter[1], Wayne Bosze[2], Shannon C. Gott[3], Bum Sung Kim[4], Masaru P. Rao[1,3], Nosang V. Myung[2], Jin Nam[1]

[1]Department of Bioengineering, University of California – Riverside, Riverside, CA 92521

[2]Department of Chemical and Environmental Engineering, University of California – Riverside, Riverside, CA 92521

[3]Department of Mechanical Engineering, University of California – Riverside, Riverside, CA 92521

[4]Korea Institute of Industrial Technology (KITECH), Incheon 406-840, Korea

*corresponding author

Jin Nam, Ph.D.

Department of Bioengineering

University of California-Riverside

900 University Ave., Riverside, CA 92521

E-mail address: jnam@engr.ucr.edu

Phone: 951-827-2064

Abstract

Piezoelectricity-based energy harvesting from wasted mechanical energies has garnered an increasing attention as a clean energy source. Especially, flexible organic piezoelectric materials provide an opportunity to exploit their uses in the mechanically challenging areas where brittle inorganic counterparts have mechanical limitations. In this regard, electrospinning has shown its advantages of producing poly(vinylidene fluoride) (PVDF)-based nanofibrous structures without the necessity of a secondary processing to induce/increase piezoelectric properties. However, the effects of electrospun fiber dimension, one of the main morphological parameters in electrospun fibers, on piezoelectricity have not been fully understood. In this study, two dependent design of experiments (DOEs) were utilized to systematically control the dimensions of electrospun poly(vinylidene fluoride-trifluoroethylene) (P(VDF-TrFE)) to produce nanofibers having their diameter ranging from 1000 to sub-100 nm. Such a dimensional reduction resulted in the increase of piezoelectric responsible electroactive phase content and the degree of crystallinity. These changes in crystal structure led to approximately 2-fold increase in piezoelectric constant as compared to typical P(VDF-TrFE) thin films. More substantially, the dimensional reduction also increased the Young's modulus of the nanofibers up to approximately 80-fold. The increases in piezoelectric constant and Young's modulus collectively enhanced piezoelectric performance, resulting in the exponential increase in electric output of nanofiber mats when the fiber diameters were reduced from 860 nm down to 90 nm. Taken together, the results suggest a new strategy to improve the piezoelectric performance of electrospun P(VDF-TrFE) via optimization of their electromechanical and mechanical properties.

Introduction

Piezoelectric materials have generated a growing interest in the diverse field of electromechanical applications for their ability to reciprocally link mechanical and electrical energies. Under the direct piezoelectric effect, an external mechanical stress induces a charge separation on the material's surface, whereas the reverse effect allows the material to exhibit a mechanical strain in response to an applied external electric field.[1] The growing demand for clean and renewable energy sources has driven the interest in developing "green" materials and systems based on such novel material characteristics for ambient energy harvesting. For example, various configurations of devices comprised of piezoelectric materials have demonstrated their ability to harvest unutilized mechanical energies.[2-5]

Inorganic materials, such as barium titanate ($BaTiO_3$), zinc oxide (ZnO), and lead zirconate titanate (PZT), are known to exhibit the highest piezoelectric responses.[6, 7] Despite their superior electromechanical response, however, these inorganic materials are brittle, therefore imposing mechanical limitations for a wide range of energy harvesting applications. In contrast, organic piezoelectric materials are mechanically resilient, providing an alternative for addressing this issue. Both polyvinylidene fluoride (PVDF), and its derivatives (*e.g.,* poly(vinylidene fluoride-trifluoroethylene (P(VDF-TrFE)), are semi-crystalline polymers that possess piezoelectric characteristics due to the polar carbon fluorine domains.[8, 9] PVDF normally settles in its *α*-phase which is composed of chain conformation in the trans (T) and gauche (G) linkages (*i.e.*, TGTG'). In order to produce the piezoelectric effect, PVDF has to be poled into its electroactive phases, either its more pronounced *β*-phase containing all trans conformation (*i.e.,* TTTT) and/or *γ*-phase (T_3GT_3G') by physical stretching and/or exposing the linkages to a strong electric field.[10] The electroactive phases allow for permanent dipoles within macroscopic domains, for which unidirectional re-orientation under a physical stress or an electric field leads to the development of a net surface charge accumulation. Trifluoroethylene residues in the copolymer, P(VDF-TrFE), act as steric hindrance stabilizers to form the *β*-

phase[11] which minimizes the necessity for extra processing (*i.e.,* physical stretching) to attain piezoelectric properties albeit such a post-process can further enhance piezoelectricity.[12]

In this context, electrospinning is advantageous to produce high performance piezoelectric polymers because the technique intrinsically subjects the polymers to a high electric field. A charged polymer jet under an electric field is attracted to a collection plate, resulting in the formation of a fibrous structure whose dimensions are controlled from a few microns down to several nanometers in diameter. During the process, the fibers are also subjected to a mechanical stretching/poling due to polymer jet elongation and whipping, further enhancing piezoelectricity. Indeed, it has been shown that electrospinning enhances piezoelectric properties of P(VDF-TrFE)[9], and even induces piezoelectricity in PVDF without the typically required post-poling process.[13]

The capacity of a piezoelectric material is commonly represented by electric charge separation and mathematically represented by the constitutive piezoelectric strain-charge equation,

$$D_i = d_{ij}\sigma_j = d_{ij}E_{kj}\varepsilon_k, \tag{1}$$

where D_i is the electric charge separation, d_{ij}, the piezoelectric coefficient, σ_j, the applied stress, E_{kj}, the Young's modulus, ε_k, the applied strain. Intuitively from the equation, changes in d_{ij} and/or E_{kj} would effectively modulate charge separation and affect the efficiency of energy harvesting. Thus far, most studies aimed to enhance piezoelectricity via modulation of the piezoelectric coefficient, d_{ij}, by novel material development. Examples include polymer-based piezocomposite materials with inorganic piezoelectric materials[14, 15] or multiwalled carbon nanotubes.[16] In spite of an equivalent contribution from E_{kj} to the overall piezoelectric response, the mechanical aspects of piezoelectric materials are often neglected.

It has been recently demonstrated that the energy conversion efficiency of electrospun PVDF is superior to that of thin films of the same thickness, and it is further enhanced by

decreasing fiber diameter.[17] The enhancement was proposed to arise from a few possible factors, including fewer defects due to a higher degree of crystallinity, size-dependent flexoelectricity, or nonlinear extrinsic responses known as domain wall motion.[17] These phenomenological observations provide critical information regarding methodologies to further enhance the performance of electrospun organic piezoelectric materials, yet the fundamental mechanisms are still elusive. Herein, we take a systematic approach to precisely control the fiber diameter of electrospun P(VDF-TrFE) ranging from approximately 1000 nm down to 70 nm. We then investigated the electric output of fibrous mats composed of these nanofibers by subjecting them to precisely controlled mechanical strains. To determine the underlying mechanisms of dimensional dependency of piezoelectricity, we examined both electromechanical and mechanical behaviors of electrospun P(VDF-TrFE) at the single fiber level by experimentally measuring the piezoelectric constant (d_{33}) and elastic modulus (E). Finally, an analysis of the phase and crystallinity content provides further explanation as to the enhanced piezoelectric response we observe with nanofibers having fiber diameter below 100 nm. The results provide a guide to design efficient piezoelectric energy harvesting devices utilizing electrospun nanofibers.

Experimental

Synthesis of electrospun P(VDF-TrFE)

P(VDF-TrFE) (70/30 mole%) (Solvay Group, France) was dissolved in a 60/40 vol. ratio of *N-N* dimethylformamide to acetone (Fisher Scientific, Pittsburgh, PA) at various polymer concentrations. For select solutions, pyridinium formate buffer (PF) (Santa Cruz Biotechnology, Dallas, TX) was added at the indicated concentrations. All solutions were magnetically stirred for 1 hr until the solution was visually transparent.

Each solution was separately loaded into a 10 ml syringe attached with a 250 μm inner diameter needle. The solution feed rate was controlled at 0.5 ml/hr by a syringe pump (New Era

Pump Systems, Inc., Farmingdale, NY). The solution was negatively charged at 14 kV by a high

voltage supply (Glassman High Voltage, Inc., High Bridge, NJ). A metal collection substrate was

placed 20 cm from the needle, and positively charged at a fixed voltage of 0.5 kV for all

conditions. Environmental conditions were kept constant at 24 °C and absolute humidity of 7.6

g/m^3.

Characterization of electrospinning solutions and resulting nanofibers

The viscosity, electrical conductivity, and surface tension of the electrospinning solutions were

characterized by a viscometer (Brookfield Engineering Laboratories, Inc., Middleboro, MA), a 4-

cell conductivity probe (Fisher scientific, Pittsburgh, PA) and a tensiometer (Scientific Gear

LLC, Fairfax, VA), respectively. The morphology of resulting electrospun nanofibers from the

solutions were characterized using a VEGA3 scanning electron microscope (SEM) (Tescan

Brno, Czech Republic). Fiber diameter (n=30) and bead density were assessed using ImageJ

software.

Electric output measurements of electrospun nanofiber mats

Electrsospun P(VDF-TrFE) having four different average fiber diameters (approximately 90,

166, 242, and 859 nm) were separately collected at a thickness of approximately 20 µm. A

cantilever set up was adopted to induce a controlled strain on the fiber samples (**Fig. 1a**).[18, 19]

The cantilever was composed of a 7.2x 1.6 x 0.01 cm^3 brass shim covered on both sides with

polyimide tape to electrically isolate it from the electrical system. A 1 x 1 cm^2 sample was cut

from the 20 µm thick electrospun nanofiber mat and fixed to the center of the cantilever with

double sided copper tape which served as the bottom-contact electrode while a similar size

aluminum foil was used as the top electrode. Two separate 24 gauge wires were fixed to the

contacts, sealed with a strip of polyimide tape, and led to a breadboard with inputs to an

oscilloscope (Lecroy, Chestnut Ridge, NY) to measure the output voltage from the nanofiber mat.

Cantilever bending was enhanced by attaching a 2.3 g proof mass at the end of the cantilever and driven by a custom-made vibrational system (**Fig. 1b**). The system utilizes a cantilever holder mounted on the top of the diaphragm of a subwoofer speaker. An ACC103 accelerometer (OMEGA Engineering, Inc., Stamford, CT) and a GoPro Hero3+ (GoPro, Inc., San Mateo, CA) were also fixed on the surface, to correlate the vibrational acceleration to cantilever surface strain which was calculated by,

$$Strain \% = \frac{t/2}{R} \times 100, \tag{2}$$

where t is the thickness of the assembled cantilever, and R is the radius of curvature of a circle overlaid on the curved cantilever surface, measured by the video camera (**Fig. 1c**).[20] A sinusoidal sound wave with controlled frequency and amplitude was delivered to the speaker via a custom LabVIEW VI. 10 Hz was the resonance frequency of the cantilever set-up determined through a frequency sweep test at a fixed acceleration of 30 m/s^2 (**Fig. 1d**). This frequency was kept constant for all subsequent experiments.

Total current (I_{total}) measurements were conducted by measuring the voltage drop (V) across the total resistance ($R_T = \frac{R_I R_L}{R_I + R_L}$) of the circuit and utilizing the current equation, $I_{total} = \frac{V}{R_T}$, where R_I is the internal resistance of the oscilloscope (10 MΩ) and R_L is a varying load resistor resulting in R_T to be 0.5, 0.9, 1.7, 3.3, 6.88, or 10 MΩ. Similarly, power (P) was calculated by $P = \frac{V^2}{R_T}$.

To demonstrate the feasibility of real-world applications of the device from a common source of wasted energy, the assembled cantilever was mounted on a side-mirror of a moving vehicle and exploited the resulting air-flow around the vehicle for energy generation.

Measurement of the output voltage was recorded using an oscilloscope powered by a power inverter connected to an amplifier in the vehicle.

Determination of piezoelectric constant using piezoresponse force microscopy (PFM)

To measure the piezoelectric constant of individual fibers, P(VDF-TrFE) nanofibers were sparsely collected on a gold coated silicon (Si) substrate during electrospinning. A MFP-3D AFM (Asylum Research, Santa Barbara, CA) in tapping mode was used to first visualize and locate individual fibers, followed by precise placement of the AFM tip on a fiber. The AFM was then switched to PFM mode where single point measurements were conducted by applying an alternating step voltage to the AFM cantilever (AC240TM, Olympus). Contact resonance was used to amplify the responding signal. At least, five independent fibers were tested at five different locations along the fiber length for each condition. Thick P(VDF-TrFE) film (80 µm) was synthesized by drop-casting a 15 wt.% P(VDF-TrFE) in acetone solution onto a gold coated Si substrate and utilized as a reference.

Mechanical characterization of individual electrospun nanofibers

A nanoscale three-point flexural test was used to determine the Young's modulus of individual nanofibers having different fiber diameters. To serve as a support for the suspended fiber, trench grated Si substrates were microfabricated as described elsewhere.[21] Briefly, the grated patterns, placed on the Si surface by photolithography, were transferred into the Si substrate using a fluorine-based dry etching process. Each Si chip contained 0.5, 0.75, 1, 2.5, 5, 10, 25, and 50 µm trenches that are specifically designed for the proper gap distance for measuring the mechanical properties of a fiber with a particular fiber diameter.

Electrospinning on the patterned Si substrate was conducted similar to the fiber collection for PFM. After fiber deposition, the AFM was first used in tapping mode to map the location of a suspended fiber across a trench having a desired separation, followed by precise

placement of the AFM tip at the center of the suspended fiber. The AFM was then switched to force mode to collect force-displacement curves. The extension and retraction speed of the AFM cantilever (AC160TS, Olympus) was fixed at 5 μm/s and the trigger force for each measurement was set at 1 μN.

In order to calculate the Young's modulus (E) from AFM force-displacement curves, Euler's beam theory was used by relating the force (F), indentation (δ), fiber suspension length (L), and fiber polar moment of inertia (I) in the equation,

$$E = \frac{L^3\left(F/\delta\right)}{48I} \ .$$
(3)

Fiber radius (r) is taken into account in the inertia terms such that,

$$I = \frac{\pi r^4}{4} \ .$$
(4)

Equation 3 accounts for non-fixed ends at the ends of the fiber suspension length.[22] The trench size was selected for each fiber such that the ratio between suspension length and fiber diameter (D) was greater than 16 (*i.e.,* L/D > 16) in order to minimize the effects of shear forces in the force measurements.[23]

Phase and crystallinity content determination of electrospun fibers

Fourier transform infrared spectroscopy (FTIR) of electrospun nanofibers was conducted to quantify phase changes depending on nanofiber diameter with an Equinox 55 FTIR spectrometer (Bruker Corp., Billerica, MA) in absorbance mode from 600 to 1600 cm^{-1}. Five spectrums per condition were collected and averaged. The electroactive phases (*β-* and *γ-*

phase) percentage was calculated by the following equation utilizing the measured absorbance spectrum,

$$EA\% = \frac{A_{EA}}{1.3A_\alpha + A_{EA}} \times 100 \tag{5}$$

where A_{EA} is the absorbance value at 841 cm^{-1}, A_α is the absorbance at 764 cm^{-1}, and the factor 1.3 is the ratio of absorption coefficients at 841 cm^{-1} (K_{841}= 7.7x10^4 cm^2 mol^{-1}) to 764 cm^{-1} (K_{764} = 6.1x10^4 cm^2 mol^{-1}) at the respective wavenumber.[24]

The degree of crystallinity of electrospun P(VDF-TrFE) nanofibers having various fiber diameters was calculated from X-ray diffraction (XRD) spectra collected with an Empyrean X-ray diffractometer (PANalytical, Almelo, the Netherlands) at 2θ from 10 - 27°, through the summation of integrated area under each crystallinity phase (α, β, and γ) over the total summation of integrated area under both crystallinity and amorphous. [25, 26]

Results and discussion

In order to correlate the electromechanical and mechanical properties of P(VDF-TrFE) nanofibers as a function of fiber dimension, we first set out to precisely control the electrospun fiber dimensions and eliminate defects (*i.e.,* beads) through a systematic approach using statistics-oriented design of experiments (DOEs). A two-level full factorial design with two factors (*i.e.,* P(VDF-TrFE) and PF solution concentrations) was designed. This requires four experimental runs, with factor analysis focusing on fiber diameter and bead density (**Table 1**). A fifth run was added to the design to serve as a center point to potentially reveal any second order quadratic effects, deviating from the general linear model on fiber diameter and bead density.

The initial low (-) and high (+) values of each design factor were empirically determined. The high P(VDF-TrFE) concentration was set based on a solution that exhibited a stable Taylor cone during electrospinning (*i.e.,* 15 wt.%), while the low concentration was determined from a solution that exhibited an unstable Taylor cone with bead formation (*i.e.,* 7 wt.%). A high PF concentration of 1 wt.% was determined from a solubility limit test when PF was mixed with the P(VDF-TrFE) solution while the low limit was set to 0 wt.%. The center point solution was synthesized at 11 wt.% P(VDF-TrFE) and 0.5 wt.% PF. The five solutions showed the expected trends in solutions properties, including concentration-dependent solution viscosity and electrical conductivity with a relatively stable surface tension (**Table 1**). Electrospinning the five solutions at the fixed electrospinning parameters resulted in various fiber morphologies (**Fig. 2**). Without or with the presence of PF, the high concentration of P(VDF-TrFE) resulted in uniform fibers with smooth surfaces with average fiber diameters of approximately 375 and 457 nm, respectively (**Fig. 2a and Fig. S1a; Fig. 2b and Fig. S1b**). When the P(VDF-TrFE) concentration was reduced to 7 wt.% in the absence of PF, thus effectively reducing the solution viscosity, electrospinning produced smaller fiber diameters of approximately 177 nm (**Fig. 2c and Fig. S1c**). However, these fibers exhibited bead formation possibly caused by the unbalance between the viscoelastic and electrical properties of the solution leading to Taylor cone instability.[27] The addition of 1 wt.% PF to the same 7 wt. % P(VDF-TrFE) solution composition effectively increased solution conductivity from 3.2 to 30.4 µS/cm and eliminated the formation of beaded fibers, but it increased the fiber diameter from 177 nm to approximately 208 nm (**Fig. 2d and Fig. S1d**). Electrospinning of the center point solution produced fibers with an average diameter of approximately 255 nm, yielding a curvature (quadratic term) of 49 nm or about 16% below the expected (linear) value (304 nm) given by averaging the 4-corners (**Fig. 2e and Fig. S1e**).

The factor analysis showed that P(VDF-TrFE) concentration exerts the greatest effect on fiber diameter, as demonstrated by the stiffest slope in the main effect plot (**Fig. 2f and Fig.**

S1f). Additionally, the direction of the slope indicates that a decrease in fiber diameter is achieved by decreasing P(VDF-TrFE) concentration. PF concentration also had an effect on fiber diameter, albeit to a significantly lesser extent than P(VDF-TrFE) concentration. The combination of the two factors has a less of an effect on fiber diameter as compared to P(VDF-TrFE) concentration . In addition, factor analysis revealed that both P(VDF-TrFE) concentration and PF concentration are highly influential to bead density (**Fig. 2g and Fig. S1g**). The increased concentration of the factors have a similar effect in magnitude and manner, exhibiting a decrease in bead formation. Unlike fiber diameter, the interactions between the two factors significantly affected the bead density. For example, it is necessary to increase the PF concentration in order to prevent bead formation when the P(VDF-TrFE) concentration is lowered to promote the reduction of fiber dimensions. These results collectively indicate that both P(VDF-TrFE) and PF concentrations should be addressed accordingly to yield the desired fiber diameter and morphology.

Based on these observations, a second DOE was designed to further reduce fiber size while limiting the bead formation (**Table 2**). The low and high values for each P(VDF-TrFE) and PF concentrations were set at 7 and 2 wt.% and 1 and 1.5 wt.%, respectively. Similar to the first DOE, the lower bound concentration of P(VDF-TrFE) was determined by the Taylor cone instability and formation of beads at the set low value of 1 wt.% PF. The upper-bound limit of PF concentration was tested for solubility in the P(VDF-TrFE) solution. A center point solution consisting of 4.5 wt.% P(VDF-TrFE) and 1.25 wt.% PF was also included. Similar to the previous sets of solutions in the first DOE, only the solution viscosity and electrical conductivity were affected by the changes in the factors. The difference in the viscosity of sample 4 from DOE 1 and that of sample 1 from DOE 2 is noted. This is due to the additional adjustment of water content depending on the amount of added PF concentration.

SEM imaging of the DOE 2 fibers showed a decrease in the average fiber diameter by decreasing the P(VDF-TrFE) concentration from 7 wt.% (approximately 405 nm at 1 wt.% PF,

481 nm at 1.5 wt.% PF) (**Fig. 3a and Fig. S2a; 3b and Fig. S2b**) to 2 wt.%-1 wt.%PF (approximately 71 nm), but with bead formation (**Fig. 3c and Fig. S2c**). Increasing the PF concentration to 1.5 wt. % at the low concentration of P(VDF-TrFE) led to the elimination of beads with an average fiber diameter of approximately 67 nm (**Fig. 3d and Fig. S2d**). The center point solution produced fibers with an average diameter of approximately 197 nm, yielding a curvature (quadratic term) of 59 nm or about 23% below the expected (linear) value (256 nm) given by averaging the 4-corners. (**Fig. 3e and Fig. S2e**). Similar to the first factor analysis, decreasing P(VDF-TrFE) concentration leads to a decrease in fiber diameter (**Fig. 3f and Fig. S2f**) while increasing PF concentration prevents bead formation (**Fig. 3g and Fig. S2g**). The effect of PF concentration on fiber diameter was significantly reduced as compared to that in the first DOE, in this fiber size range. The effects of both individual factors and interactions between the factors on bead density were similar to the results in the first DOE. Considering that the used PF concentration is the maximum allowed for complete solubility, the resulting fiber size from 2 wt.% P(VDF-TrFE) concentration is likely in the range of the smallest fiber sizes that can be produced without the bead formation in this polymer-solvent system.

After establishing a means to precisely control fiber diameter, the electrospun P(VDF-TrFE) nanofiber mats of various fiber diameters were investigated to determine size-dependent piezoelectric properties under controlled strains. Five separate cantilevers each with either 90, 166, 242, and 859 nm average fiber diameter mats were tested in the custom vibrational system. At a fixed frequency of 10 Hz and surface strain of 0.18%, the results showed that the voltage generation was exponentially increased by decreasing the fiber diameter fibers especially below approximately 200 nm (**Fig. 4a and Fig. S3**). At a maximum peak-to-peak voltage of approximately 700 mV, this value exceeds the reports from other studies.[7, 28] It should be noted that the electric output of piezoelectric materials strongly depends on many factors such as test-measurement set up and strain rate, making a direct comparison difficult.[29, 30]

Determination of the maximum peak-to-peak total current (**Fig. 4b**) and maximum peak-to-peak power (**Fig. 4c**) outputs for each nanofiber mat required measuring the voltage drop across a total resistance which was adjusted by varying the load resistor (**Fig. S4**). The potential drop across each total resistance increased as the load was increased from 0.5 MΩ to an open circuit potential (i.e., ∞ MΩ). This behavior is expected since the induced charge separation from the piezoelectric nanofiber mat is greater for larger resistance values. Further analysis showed that the current and power outputs are also fiber size dependent where each measured fiber diameter has an optimum output at a particular total resistance. The maximum peak-to-peak total current and peak-to-peak power (calculated from **Fig. S5**)**,** for each nanofiber mat having different fiber size is plotted in **Fig. 4b and 4c**. This indicates that, in addition to the fiber diameter, total resistance in the system can be adjusted to meet power requirements.

Additionally, translation of the cantilever assembly to a real world application demonstrates the potential of utilizing the nanofibers for harvesting wasted energy (**Fig. 5**). By mounting the piezoelectric cantilever on the surface of a moving vehicle, the mechanical strain produced by the wind turbulence generated approximately 2.5 V_{p-p} from the cantilever containing the 90 nm average diameter nanofiber mat (**Fig. 5c**).

To elucidate the underlying mechanisms governing the dimension dependent piezoelectricity of electrospun P(VDF-TrFE) nanofibers, electromechanical and mechanical properties were investigated at the single fiber level. As shown in the constitutive strain-charge piezoelectric equation (Equation 1), the electrical response of a piezoelectric material depends on the intrinsic piezoelectric coefficient (*d*), Young's modulus of the material (*E*), and an applied strain (*ε*). Equation 1 can be further derived to describe the output voltage (V) of varying fiber sizes through the voltage equation[31]

$$V = \frac{D_3 d}{k} = \frac{[d_{33}\sigma_3\,]d}{k} = \frac{[d_{33}(E_{33}\varepsilon_3)\,]d}{k}, \tag{6}$$

where k is the permittivity of the material and d is the charge separation distance (*i.e.,* fiber diameter). Equation 6 indicates that the piezoelectric coefficient, Young's modulus of the material and nanofiber diameter collectively determine electric output of the electrospun P(VDF-TrFE) at a particular dimension.

The fiber size dependent d_{33} values were determined by PFM (**Fig. 6**). The PFM phase response image showed a relatively uniform color distribution across the fiber surface, indicating a uniaxial oriented dipole moment as expected from other studies that demonstrated polarization of PVDF by electrospinning[32] (**Fig. 6a**). PFM imaging in amplitude mode also showed a relatively uniform amplitude response across the same fiber (**Fig. 6b**). It should be noted that due to the triangular nature of the AFM tip, in-plane scanning leads to a common artifact which makes a fiber appear to be larger in width than the measured fiber diameter through other methods such as SEM, as described by Schneider et al.[28] Therefore, only the out-of-plane height value was used to properly determine the actual fiber diameter during the PFM measurements. To determine the piezoresponse of the fibers in more detail, individual fibers were subjected to single point piezoresponse spectroscopy in contact mode. Under an applied step voltage (top), representative raw signals of a PFM measurement shows the phase (middle) and amplitude (bottom) responses of a P(VDF-TrFE) fiber (**Fig. 6c**). Due to the direction of the electric field of our electrospinning set up (*i.e.,* from the positive collection plate to a negative spinneret) we expected the dipole orientation of electrospun P(VDF-TrFE) domains to be perpendicular to, and pointing away from, the collection surface. As expected, the phase response shows a 180 degree orientation switch in dipole moment when a positive bias is applied while a 0 degree response was observed when a negative bias is applied. Amplitude response, however, remains the same in magnitude regardless of the polarity of the applied voltage.

Similarly, the fiber dimension-dependent d_{33} of electrospun P(VDF-TrFE) fibers was determined from the amplitude response of individual fibers having different diameters. For the calculation of d_{33}, the quality factor (Q) of the AFM cantilever was taken into account since the amplitude responses were amplified by utilizing a resonance tracking technique, such that

$$d_{33} = \frac{A}{VQ},$$ (7)

where A is the amplitude and V is the applied voltage.[33] The results show that any sized electrospun P(VDF-TrFE) fibers exhibit a greater d_{33} as compared to bulk, and the fibers between 500 - 1000 nm in diameter exhibit slightly greater or equal d_{33} value as compared to thick film P(VDF-TrFE) (**Fig. 6d**). More importantly, there is a substantial increase in d_{33} when the fiber diameter decreases below 500 nm. Curve-fitting shows a linear log-log relationship between d_{33} and the inverse of fiber diameter as

$$\log d_{33} = 1.96 + 0.19 \log \frac{1}{d},$$ (8)

where d is the fiber diameter (R^2=0.89, **Fig. 6e**). To the best of our knowledge, the empirically determined maximum d_{33} perpendicular to the fiber length in this study (-56 pm/V) exceeds the reported values of PVDF (fiber:45pm/V[14]; film: 33 pm/V[34]) and P(VDF-TrFE) (film: -40 pm/V[35, 36]). This is likely due to the effects of substantial dimensional reduction that may lead to structural changes such as an increase in the electroactive phase, or lowered domain wall barriers.[7] The only comparable d_{33} (-56.7 pm/V) value was reported from a single PVDF fiber deposited by near-field electrospinning.[37] However, it should be noted that the dipole orientation of the near-field electrospun fiber runs parallel with the fiber axis, different from the

Dimensional reduction of a material typically results in the substantial increase in the material stiffness, represented by Young's modulus.[38, 39] As shown in Equation 6, such an increase in Young's modulus can significantly affect the overall charge separation, thus the piezoelectric performance. To investigate the effects of dimensional reduction on the mechanical properties of individual nanofibers, a three-point flexural test at the nanoscale was utilized (**Fig. 7**). In order to subject an individual nanofiber to the three-point bending, a Si substrate having micro-patterned trenches with well-defined gap distances was utilized (**Fig. 7a**). Individual fibers were visualized by AFM in imaging mode prior to being subjected to loading by the AFM in force mode (**Fig. 7b**). A representative force-displacement curve from these measurements is shown in **Fig. 7c**. A linear region of the extension curve from the force-displacement data was used to calculate the Young's moduli of P(VDF-TrFE) fibers of different diameters (**Fig. 7d**). The Young's moduli of the individual fibers having diameters between the range of 800 nm to 1000 nm were relatively close in value to that of bulk P(VDF-TrFE) at 1 GPa. However, fibers showed significant increase in Young's modulus as the diameter was further decreased. As shown in **Fig. 7e**, a linear log-log relationship was revealed between E and the inverse of fiber diameter (R^2=0.89) as

$$\log E = 4.89 + 1.62 \log \frac{1}{d} \ .\tag{9}$$

These results are comparable to the study in which the dimensional reduction in poly(2-acrylamido-2-methyl-1-propanesulfonic acid) (PAMPS) nanofibers exponentially increased Young's modulus from ~ 0.3 GPa to 2.0 GPa as the diameter was reduced.[39]

To understand the mechanisms underlying the fiber size-dependent increase in piezoresponse and Young's modulus of electrospun P(VDF-TrFE), electroactive phase content and the degree of crystallinity were characterized by FTIR and XRD, respectively for the selected fiber diameters (**Fig. 8 and Fig. S6**). An increase in electroactive phase formation in electrospun PVDF as compared to thick film was observed similar to the reports by others[40, 41]. Interestingly, Fig. 8a shows that the electroactive phases ratio increased as the fiber dimension decreased, which is expected to contribute to the observed increase in d_{33}. The electroactive content of the electrospun P(VDF-TrFE) fibers in this study (up to approximately 89%) exhibited a similar, or higher values than the reported values in literature.[9, 16, 40, 42]

Simultaneously, the decrease in fiber diameter resulted in an increase in the degree of crystallinity (**Fig. 8b** and **Fig. S6d**). The increase in ordered microstructure of polymer chains likely contributed to the enhanced mechanical properties of the electrospun P(VDF-TrFE) fibers as has been observed for other polymer types.[43, 44] Furthermore, the predicted Young's modulus by Equation 9 can be curve-fitted to the degree of crystallinity with an R^2=0.96 as shown in **Fig. 8b**, further demonstrating the strong correlation between the crystallinity and the fiber mechanical properties. Similarly, the calculated amount of the electroactive phases (*i.e.,* the product of electroactive phases content and crystallinity) was curve-fitted by the predicted d_{33} using Equation 8 (R^2 = 0.98) since the electroactive phases of P(VDF-TrFE) is responsible for the piezoelectric properties of the polymer[32] (**Fig. 8c**). The results demonstrate a possibility of further enhancing piezoelectric properties of electrospun P(VDF-TrFE) by increasing not only the electroactive phases content but also material crystallinity.

Since both the electromechanical and mechanical properties of electrospun P(VDF-TrFE) fibers contribute to energy generation, the interaction of the two on electric output at the single fiber level as a function of fiber diameter was numerically determined and compared to the measured values (**Fig. 8d**). Equations 8 and 9, which correlate piezoelectric constant and Young's modulus to fiber diameter, were combined with Equation 6 to predict voltage generated

by a single fiber with different fiber diameters. A significant correlation was found between the predicted values of single fibers and the measure voltage values of nanofiber mats from Fig. 4a (R^2=0.84). This correlation strongly indicates that while the piezoelectric coefficient is significant in determining the electrical performance of a piezoelectric material, mechanical properties of the material equally contribute to piezoelectric efficiency.

Conclusion

In summary, a systematic approach using DOE was used to precisely control fiber size (from sub-100 nm to 1000 nm) and morphology of electrospun P(VDF-TrFE) fibers. The dependency of the electromechanical and mechanical properties of electrospun P(VDF-TrFE) on fiber size was demonstrated. Specifically, the electric output of electrospun P(VDF-TrFE) nanofiber mats strongly depended on fiber diameter with an exponential behavior, where smaller fibers exhibited greater electric output. This is likely due to the substantial increases in both piezoelectric constant (approximately 2-fold change) and Young's modulus (80-fold change) at the smaller dimensions. These findings are attributed to the combination of increases in the electroactive phase content and crystallinity by the dimensional reduction. Both the electromechanical and mechanical properties of electrospun P(VDF-TrFE) have demonstrated to be important fundamental factors in determining piezoelectric properties of the nanofibers, suggesting a new strategy to improve/optimize the piezoelectric performance of electrospun P(VDF-TrFE).

Acknowledgments

References

1.   J. Sirohi and I. Chopra, *Journal of Intelligent Material Systems and Structures*, 2000, **11**, 246-257.
2.   W. Zeng, X.-M. Tao, S. Chen, S. Shang, H. L. W. Chan and S. H. Choy, *Energy & Environmental Science*, 2013, **6**, 2631-2638.
3.   M. Lee, C.-Y. Chen, S. Wang, S. N. Cha, Y. J. Park, J. M. Kim, L.-J. Chou and Z. L. Wang, *Advanced Materials*, 2012, **24**, 1759-1764.
4.   Y. Yang, H. Zhang, G. Zhu, S. Lee, Z.-H. Lin and Z. L. Wang, *ACS Nano*, 2012, **7**, 785-790.
5.   V. Corral-Flores, D. Bueno-Baqués and R. F. Ziolo, *MRS Online Proceedings Library*, 2011, **1325**, null-null.
6.   C.-N. Xu, M. Akiyama, K. Nonaka and T. Watanabe, *Ultrasonics, Ferroelectrics and Frequency Control, IEEE Transactions on*, 1998, **45**, 1065-1070.
7.   K. Tomoaki, Y. Kang, M. Toshiyuki and A. Masatoshi, *Japanese Journal of Applied Physics*, 2007, **46**, L97.
8.   Y. R. Wang, J. M. Zheng, G. Y. Ren, P. H. Zhang and C. Xu, *Smart Materials and Structures*, 2011, **20**, 045009.
9.   L. Persano, C. Dagdeviren, Y. Su, Y. Zhang, S. Girardo, D. Pisignano, Y. Huang and J. A. Rogers, *Nat Commun*, 2013, **4**, 1633.
10.   A. Salimi and A. A. Yousefi, *Polymer Testing*, 2003, **22**, 699-704.
11.   D.-W. Kim, Lee, Gwang-Geun, Park, Byung-Eun, *Journal of the Korean Physical Society*, 2007, **51**, 719 - 722.
12.   H. L. W. Chan, Z. Zhao, K. W. Kwok, C. L. Choy, C. Alquié, C. Boué and J. Lewiner, *Journal of applied physics*, 1996, **80**, 3982-3991.
13.   H. Shao, J. Fang, H. Wang and T. Lin, *RSC Advances*, 2015, **5**, 14345-14350.
14.   A. Baji, Y.-W. Mai, Q. Li and Y. Liu, *Composites Science and Technology*, 2011, **71**, 1435-1440.
15.   J. S. Dodds, F. N. Meyers and K. J. Loh.
16.   Y. Ahn, J. Y. Lim, S. M. Hong, J. Lee, J. Ha, H. J. Choi and Y. Seo, *The Journal of Physical Chemistry C*, 2013, **117**, 11791-11799.
17.   C. Chang, V. H. Tran, J. Wang, Y.-K. Fuh and L. Lin, *Nano letters*, 2010, **10**, 726-731.
18.   L. Gu, *Microelectronics Journal*, 2011, **42**, 277-282.
19.   K.-Q. Fan, F.-B. Chao, J.-G. Zhang, W.-D. Wang and X.-H. Che, *Energy Conversion and Management*, 2014, **86**, 561-567.
20.   G. Alici and N. N. Huynh, *Sensors and Actuators A: Physical*, 2006, **132**, 616-625.
21.   P. Vandrangi, S. C. Gott, R. Kozaka, V. G. J. Rodgers and M. P. Rao, 2014.
22.   P. Zhou, C. Wu and X. Li, *Measurement Science and Technology*, 2008, **19**, 115703.
23.   W. Wang, P. Ciselli, E. Kuznetsov, T. Peijs and A. H. Barber, *Philosophical Transactions of the Royal Society of London A: Mathematical, Physical and Engineering Sciences*, 2008, **366**, 1613-1626.
24.   S. K. Ghosh, M. M. Alam and D. Mandal, *RSC Adv.*, 2014, **4**, 41886-41894.
25.   M.-C. García-Gutiérrez, A. Linares, I. Martín-Fabiani, J. J. Hernández, M. Soccio, D. R. Rueda, T. A. Ezquerra and M. Reynolds, *Nanoscale*, 2013, **5**, 6006-6012.
26.   P. Martins, A. C. Lopes and S. Lanceros-Mendez, *Progress in polymer science*, 2014, **39**, 683-706.
27.   H. Fong, I. Chun and D. H. Reneker, *Polymer*, 1999, **40**, 4585-4592.
28.   J. J. Schneider, J. Engstler, S. Franzka, K. Hofmann, B. Albert, J. Ensling, P. Gütlich, P. Hildebrandt, S. Döpner and W. Pfleging, *Chemistry-A European Journal*, 2001, **7**, 2888-2895.
29.   J. Fang, X. Wang and T. Lin, *Journal of Materials Chemistry*, 2011, **21**, 11088-11091.
30.   B. J. Hansen, Y. Liu, R. Yang and Z. L. Wang, *ACS Nano*, 2010, **4**, 3647-3652.

31.   A. Meitzler, H. F. Tiersten, A. W. Warner, D. Berlincourt, G. A. Couqin and F. S. Welsh Iii, *Journal*, 1988.

32.   D. Mandal, S. Yoon and K. J. Kim, *Macromolecular rapid communications*, 2011, **32**, 831-837.

33.   S. Xie, A. Gannepalli, Q. N. Chen, Y. Liu, Y. Zhou, R. Proksch and J. Li, *Nanoscale*, 2012, **4**, 408-413.

34.   J. Gomes, J. S. Nunes, V. Sencadas and S. Lanceros-Méndez, *Smart Materials and Structures*, 2010, **19**, 065010.

35.   A. V. Bune, C. Zhu, S. Ducharme, L. M. Blinov, V. M. Fridkin, S. P. Palto, N. G. Petukhova and S. G. Yudin, *Journal of applied physics*, 1999, **85**, 7869-7873.

36.   Y.-Y. Choi, T. G. Yun, N. Qaiser, H. Paik, H. S. Roh, J. Hong, S. Hong, S. M. Han and K. No, *Scientific reports*, 2015, **5**.

37.   J. Pu, X. Yan, Y. Jiang, C. Chang and L. Lin, *Sensors and Actuators A: Physical*, 2010, **164**, 131-136.

38.   S. Cuenot, S. Demoustier-Champagne and B. Nysten, *Physical Review Letters*, 2000, **85**, 1690.

39.   M. K. Shin, S. I. Kim, S. J. Kim, S.-K. Kim, H. Lee and G. M. Spinks, *Applied physics letters*, 2006, **89**, 231929.

40.   J. S. Andrew and D. R. Clarke, *Langmuir*, 2008, **24**, 670-672.

41.   A. Baji, Y.-W. Mai, Q. Li and Y. Liu, *Nanoscale*, 2011, **3**, 3068-3071.

42.   A. Baji, Y.-W. Mai and S.-C. Wong, *Polymer Engineering & Science*, 2015, **55**, 1812-1817.

43.   S. Y. Gu, Q. L. Wu, J. Ren and G. J. Vancso, *Macromolecular rapid communications*, 2005, **26**, 716-720.

44.   R. Jaeger, H. Schönherr and G. J. Vancso, *Macromolecules*, 1996, **29**, 7634-7636.

Table 1. **First design of experiment matrix**. Experimental design variables (P(VDF-TrFE) concentration, PF concentration) each with their respective low (-) and high (+) values and their effect on solution properties. Viscosity taken at a shear rate 90.5 s^{-1}.

Sample	Code	Design factors		Solution properties		
		P(VDF-TrFE) concentration (wt.%)	PF concentration (wt.%)	Viscosity (cP)	Electrical conductivity (µS/cm)	Surface tension (dynes/cm)
1	(+ -)	15	0.0	1255	9.69	34.4
2	(+ +)	15	1.0	2936	93.29	34.2
3	(- -)	7	0.0	60	3.22	32.3
4	(- +)	7	1.0	43	30.40	31.8
5	(o o)*	11	0.5	544	31.30	31.8

* O indicates mid-point value of each design factor

Table 2. Second design of experiment matrix. Modified experimental design variables (P(VDF-TrFE) concentration, PF concentration) each with their respective low (-) and high (+) values and their effect on solution properties. Viscosity taken at a shear rate 90.5 s^{-1}.

Sample	Code	Design factors		Solution properties		
		P(VDF-TrFE) concentration (wt.%)	PF concentration (wt.%)	Viscosity (cP)	Electrical conductivity (μS/cm)	Surface tension (dynes/cm)
1	(+ -)	7.0	1.00	72	27.92	32.8
2	(+ +)	7.0	1.50	60	54.10	34.5
3	(- -)	2.0	1.00	4	28.52	31.9
4	(- +)	2.0	1.50	4	45.22	32.6
5	(o o)*	4.5	1.25	11	37.70	34

* O indicates mid-point value of each design factor

Figure captions

Fig. 1. Custom piezoelectric actuation system. (a) A schematic showing a cantilever where electrospun P(VDF-TrFE) nanofiber mat is sandwiched between two electrodes and sealed in the middle of the beam with polyimide tape. The proof mass aids in bending the cantilever while it is clamped on the vibrating surface by a speaker (b) where an accelerometer and a video camera are also mounted. (c) The surface strain imposed on the sample is calculated by the radius of the curvature, which is captured in the video and traced with an overlaid circle on the bend of the cantilever (red dashed curve). (d) Frequency sweep from 0 to 60 Hz with respect to surface strain shows the optimum frequency at 10 Hz.

Fig. 2. Morphological characterization of electrospun P(VDF-TrFE) fibers and factor effects from the first DOE conditions. Resulting fiber morphology of 15 wt.% P(VDF-TrFE) solution with 0 wt.% (a) and 1 wt.% (b) PF, 7 wt.% P(VDF-TrFE) solution with 0 wt.% (c) and 1 wt.% (d) PF, and midpoint 11 wt.% P(VDF-TrFE) solution with 0.5 wt.% PF(e). (Scale bar = 2 µm). Effect of each design parameters, P(VDF-TrFE) concentration and PF concentration, low and high on fiber diameter (f) (n=30) and bead density (g). The red line indicates the mean value of the respective morphology.

Fig. 3. Morphological characterization of electrospun P(VDF-TrFE) fibers and factor effects from second DOE conditions. Resulting fiber morphology of 7 wt.% P(VDF-TrFE) solution with 1 wt.% (a) and 1.5 wt.% (b) PF, 2 wt.% P(VDF-TrFE) solution with 1 wt.% (c) and 1.5 wt.% (d) PF, and midpoint 4.5 wt.% P(VDF-TrFE) solution with 1.25 wt.% PF (e). (Scale bar = 2 µm). Effect of each design parameters, P(VDF-TrFE) concentration and PF concentration, low and high on fiber diameter (f) (n=30) and bead density (g). The red line indicates the mean value of the respective morphology.

Fig. 4. The effects of (a-c) fiber diameter and (d) applied strain on the electric output of electrospun P(VDF-TrFE) nanofiber mats. (a) Peak-to-peak voltage, (b) maximum peak-to-peak total current, and (c) maximum peak-to-peak power of electrospun P(VDF-TrFE) nanofiber mats having various average fiber diameter under 0.18% strain at 10 Hz. (d) Peak-to-peak voltage generation of electrospun P(VDF-TrFE) nanofiber mats having various average fiber diameter under various applied strains at 10 Hz.

Fig. 5. Wasted energy harvesting using electrospun P(VDF-TrFE) nanofibers. (a) P(VDF-TrFE) nanofibers having an average fiber diameter of 90 nm were assembled to the cantilever system and mounted on the side-view mirror of a vehicle. (b) Wires from the mounted cantilever were routed to an oscilloscope powered by a power inverter connected to an amplifier. (c) An example of the voltage generation in the electrospun P(VDF-TrFE) nanofibers mounted on a moving vehicle over a period of 200 ms.

Fig. 6. Piezoresponse force microscopy (PFM) on individual P(VDF-TrFE) nanofibers. (a) PFM contrast mapping with consistent phase response along the fiber, and (b) amplitude response of the same fiber. (c) Amplitude and phase change in response to an applied bias over time. (d) Measured d_{33} as a function of fiber diameter from point specific PFM and (e) in log-log form showing an increase in d_{33} with a decrease in fiber diameter. The red dashed line indicates the measured d_{33} of a 80 µm thick film and the black dashed line indicates the d_{33} of bulk P(VDF-TrFE). The solid red line is a linear best-fit.

Fig. 7. Young's modulus of individual fiber. (a) SEM and (b) AFM topographical image of a representative set up of the three-point bending test consisting of an individual suspended fiber across a 10 µm grating (scale bar = 5 µm). (c) Force and displacement values are extracted from AFM force curves. (d) Calculated Young's modulus as a function of fiber diameter and (e) in log-log form showing an increase in Young's modulus with a decrease in fiber diameter. The black dashed line represents the bulk Young's modulus of P(VDF-TrFE). The red solid line is a linear best-fit describing the relationship between fiber diameter and Young's modulus.

Fig. 8. Electroactive phase and degree of crystallinity, and their correlation to Young's modulus, piezoelectric constant, and electric output. (a) Electroactive phase content as a function of fiber diameter determined by FTIR. (b) Degree of crystallinity as a function of fiber diameter determined by FTIR, and its correlation to predicted Young's modulus. (c) Comparison between the dependence of predicted d_{33} and electroactive phase content on fiber diameter. (d) Comparison between empirically determined output voltage of nanofiber mats and numerically determined output voltage of a single fiber. The black dotted line in (a) and (b) indicates the measured electroactive-percentage and degree of crystallinity, respectively, of the measured drop casted thick film.
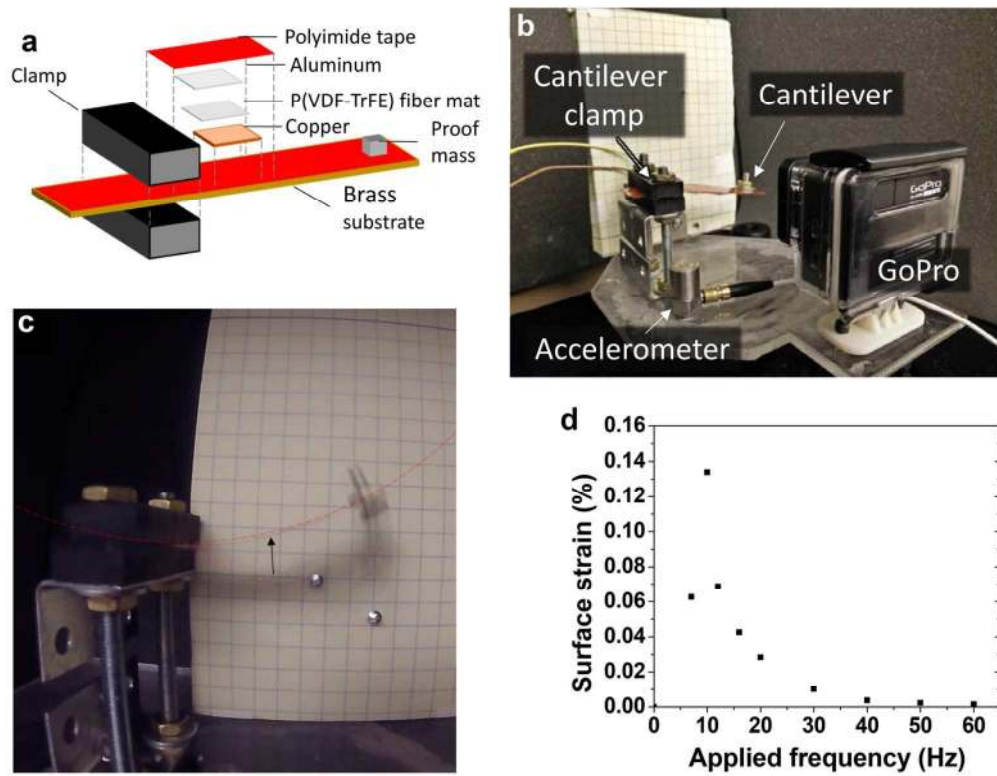
132x102mm (300 x 300 DPI)
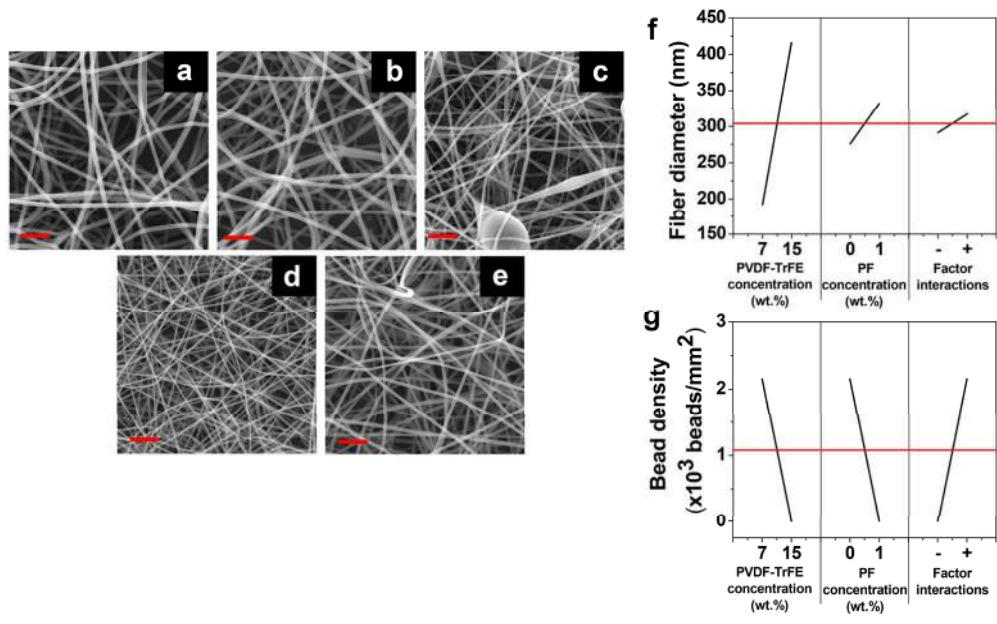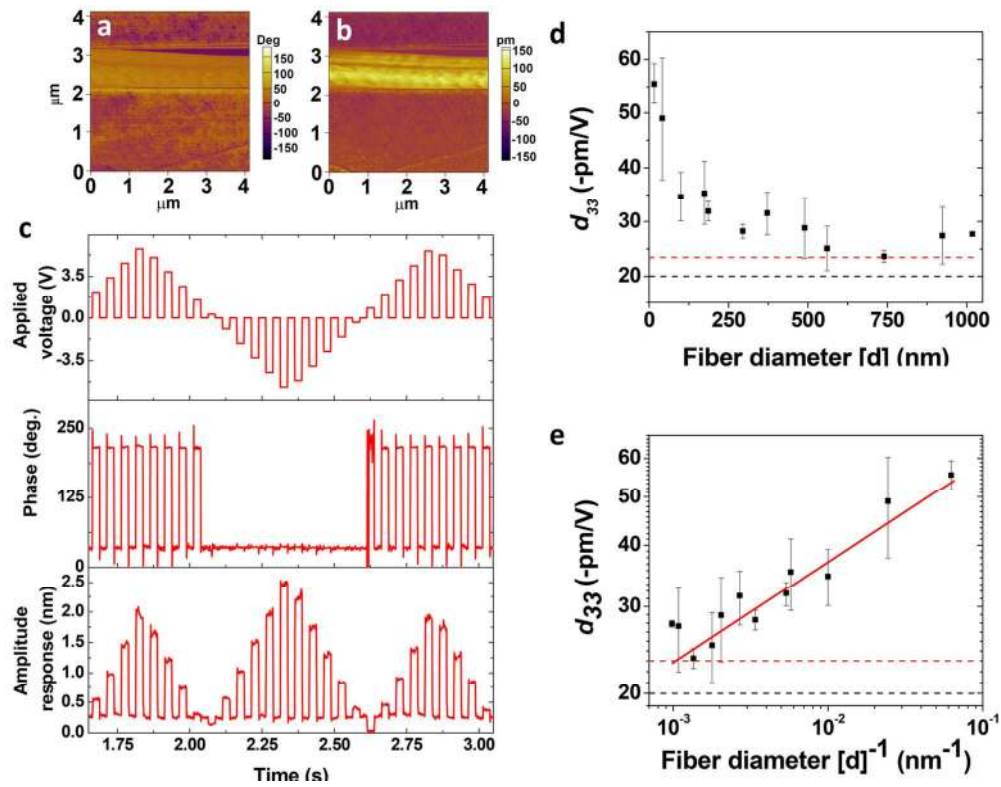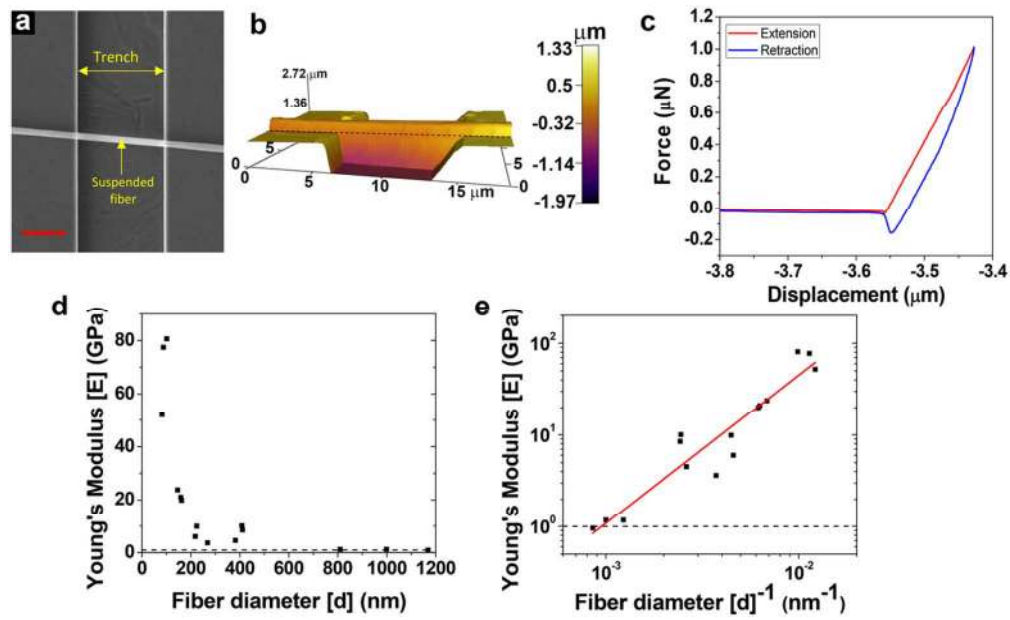
104x63mm (300 x 300 DPI)
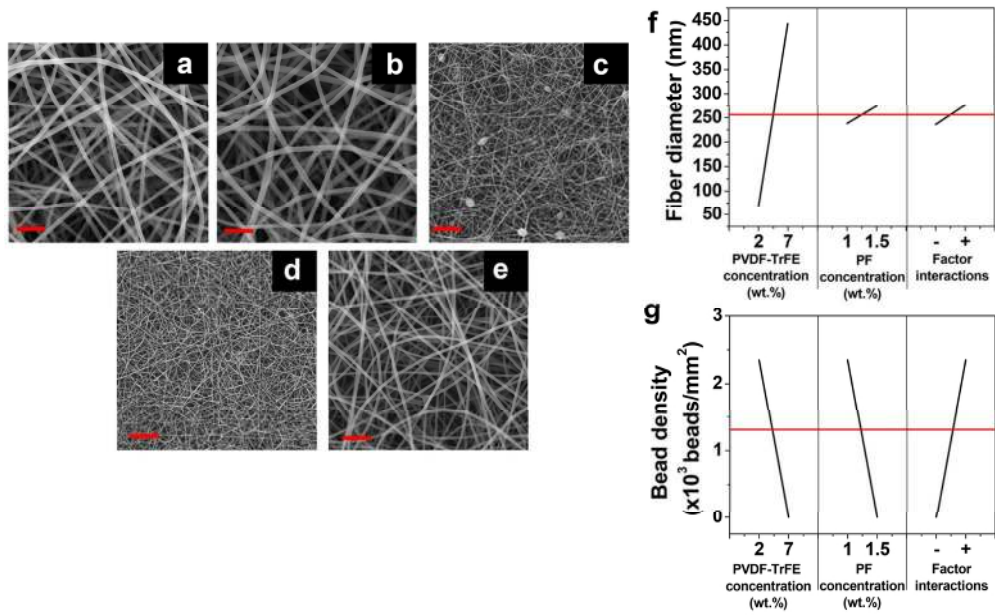
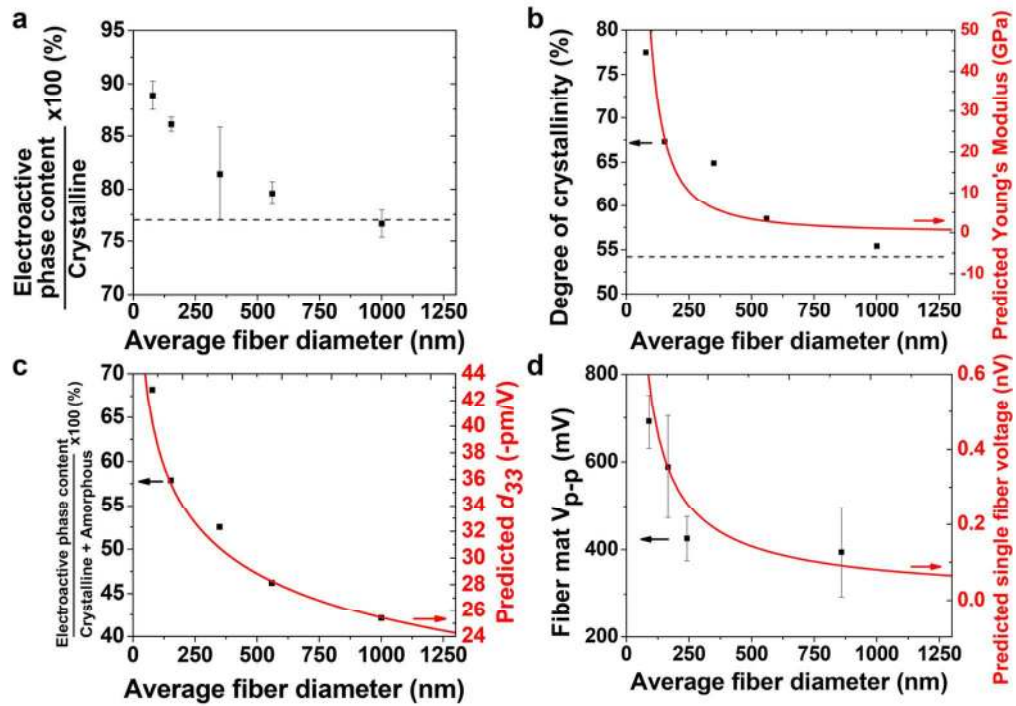104x63mm (300 x 300 DPI)
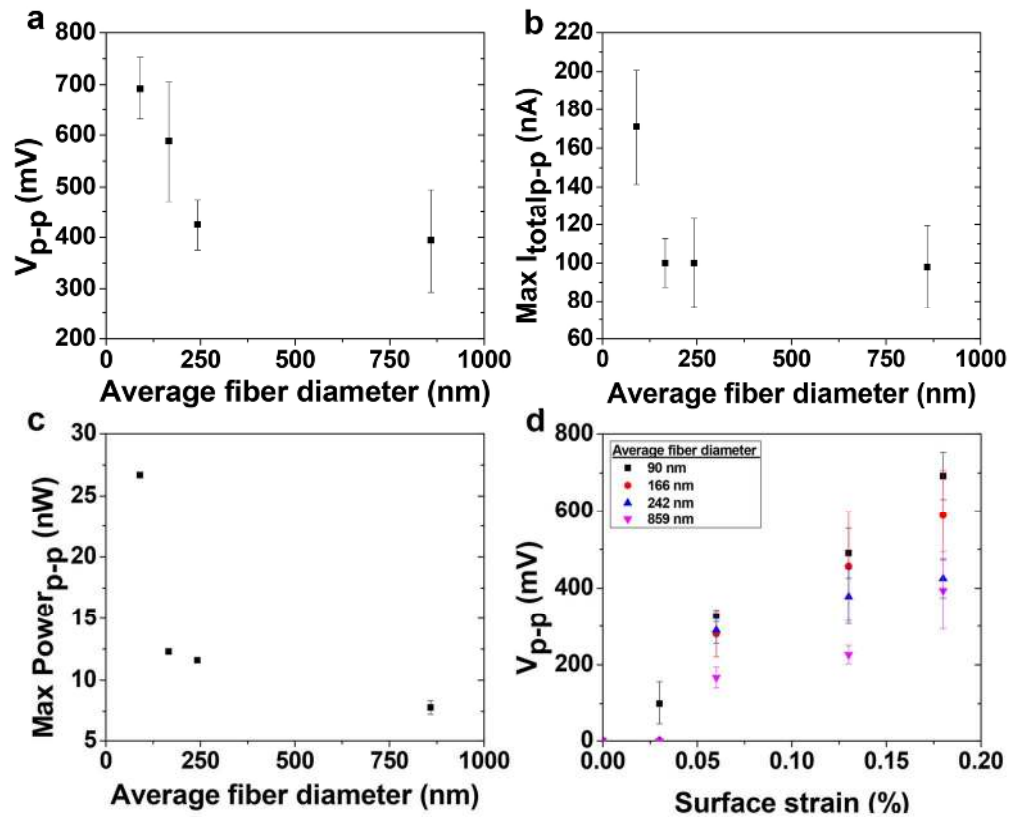
138x112mm (300 x 300 DPI)

45x12mm (300 x 300 DPI)

132x102mm (300 x 300 DPI)

104x63mm (300 x 300 DPI)
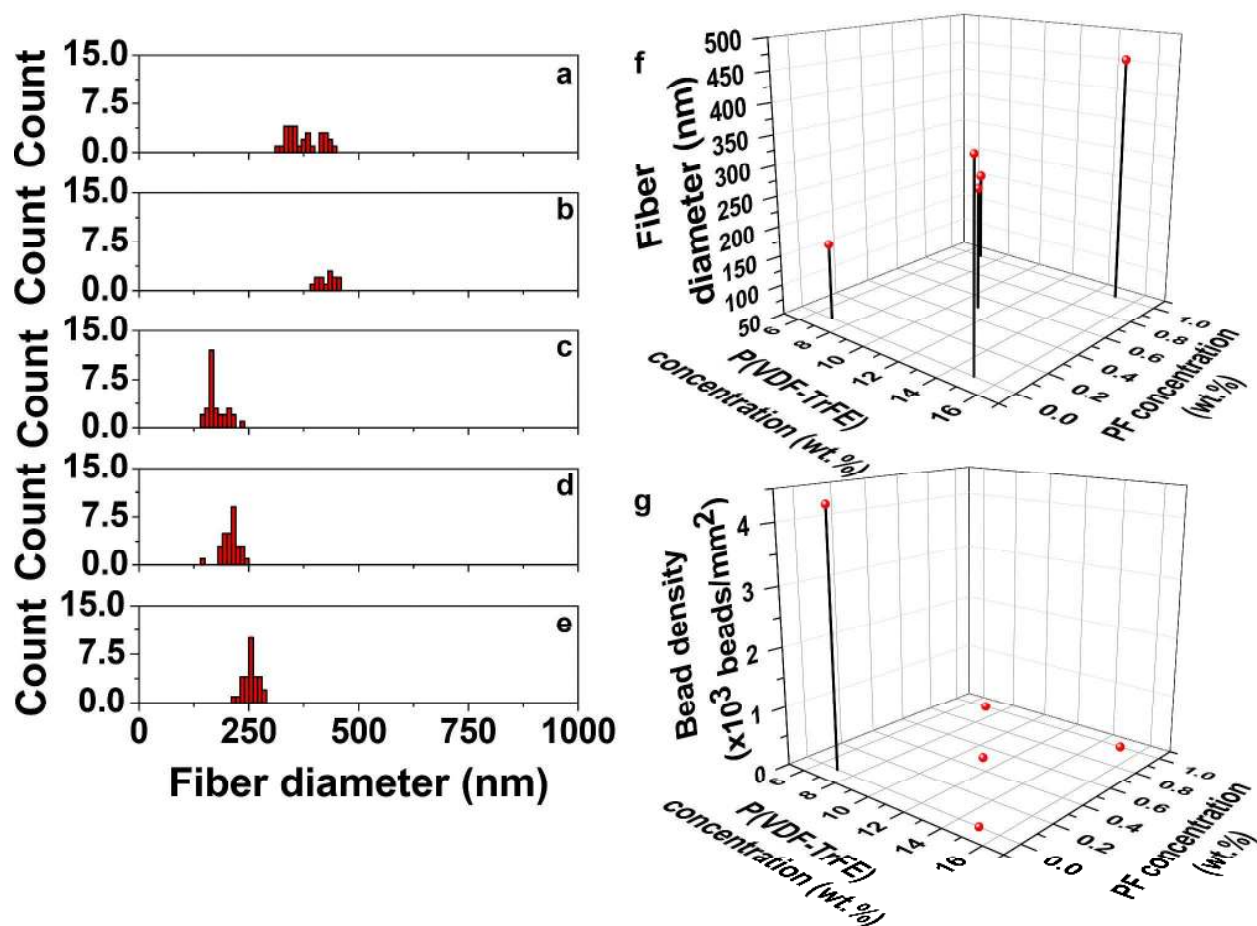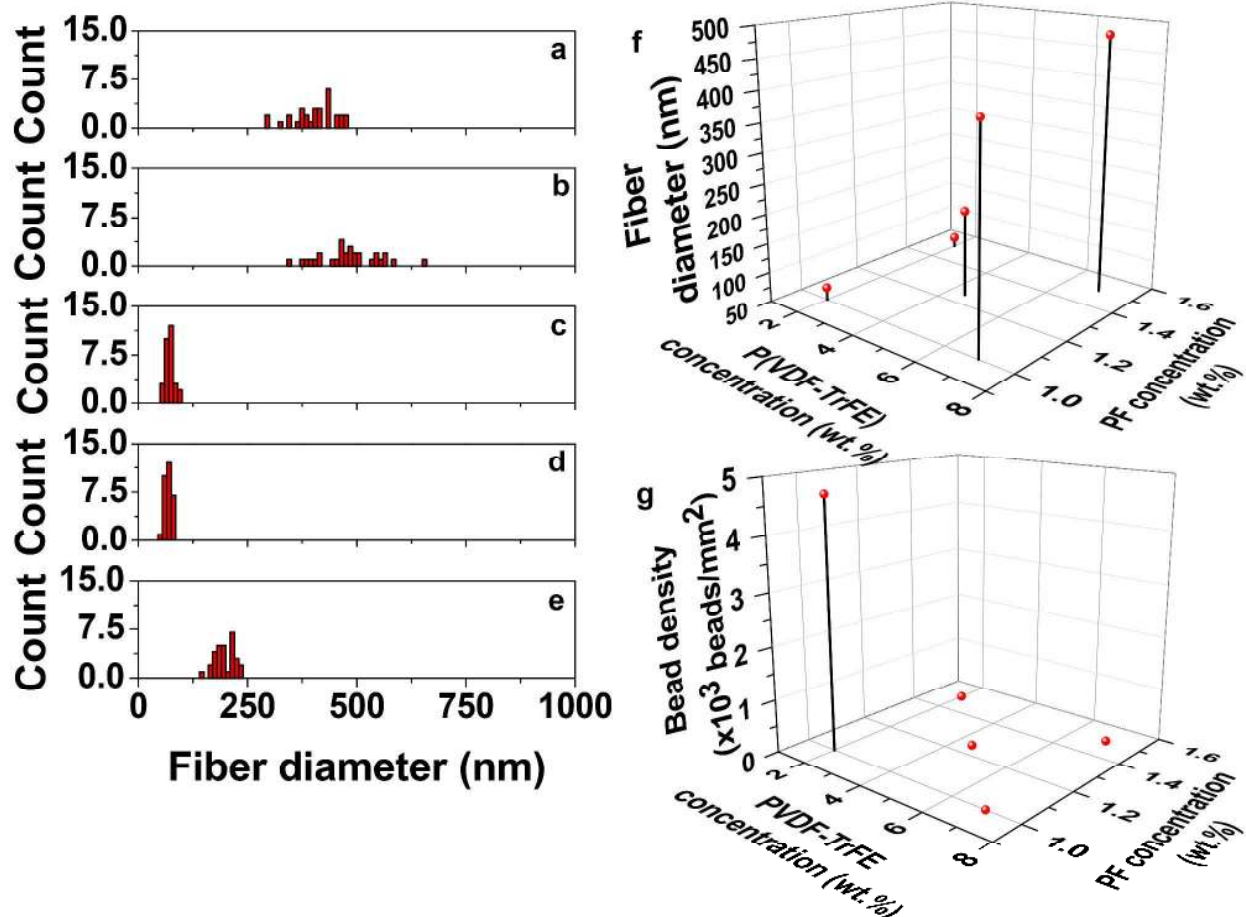
122x87mm (300 x 300 DPI)

Figure S1. Fiber diameter and bead density with respect to design parameters. Resulting fiber diameter distribution of DOE1: 15 wt.% P(VDF-TrFE) solution with 0 wt.% (a) and 1 wt.% (b) PF, 7 wt.% P(VDF-TrFE) solution with 0 wt.% (c) and 1 wt.% (d) PF, and midpoint 11 wt.% P(VDF-TrFE) solution with 0.5 wt.% PF(e). Fiber diameter (f) and bead density (g) vs design parameters, P(VDF-TrFE(concentration (15,11, and 7 wt.%) and PF concentration (0, 0.5, and 1 wt.%) (n=30).

Figure S2. Fiber diameter and bead density with respect to design parameters. Resulting fiber diameter distribution of DOE2: 7 wt.% P(VDF-TrFE) solution with 1 wt.% (a) and 1.5 wt.% (b) PF, 2 wt.% P(VDF-TrFE) solution with 1 wt.% (c) and 1.5 wt.% (d) PF, and midpoint 4.5 wt.% P(VDF-TrFE) solution with 1.25 wt.% PF (e). Fiber diameter (a) and bead density (b) vs design parameters, P(VDF-TrFE) concentration (7, 4.5, and 2 wt.%) and PF concentration (1, 1.25, and 1.5 wt.%) (n=30).
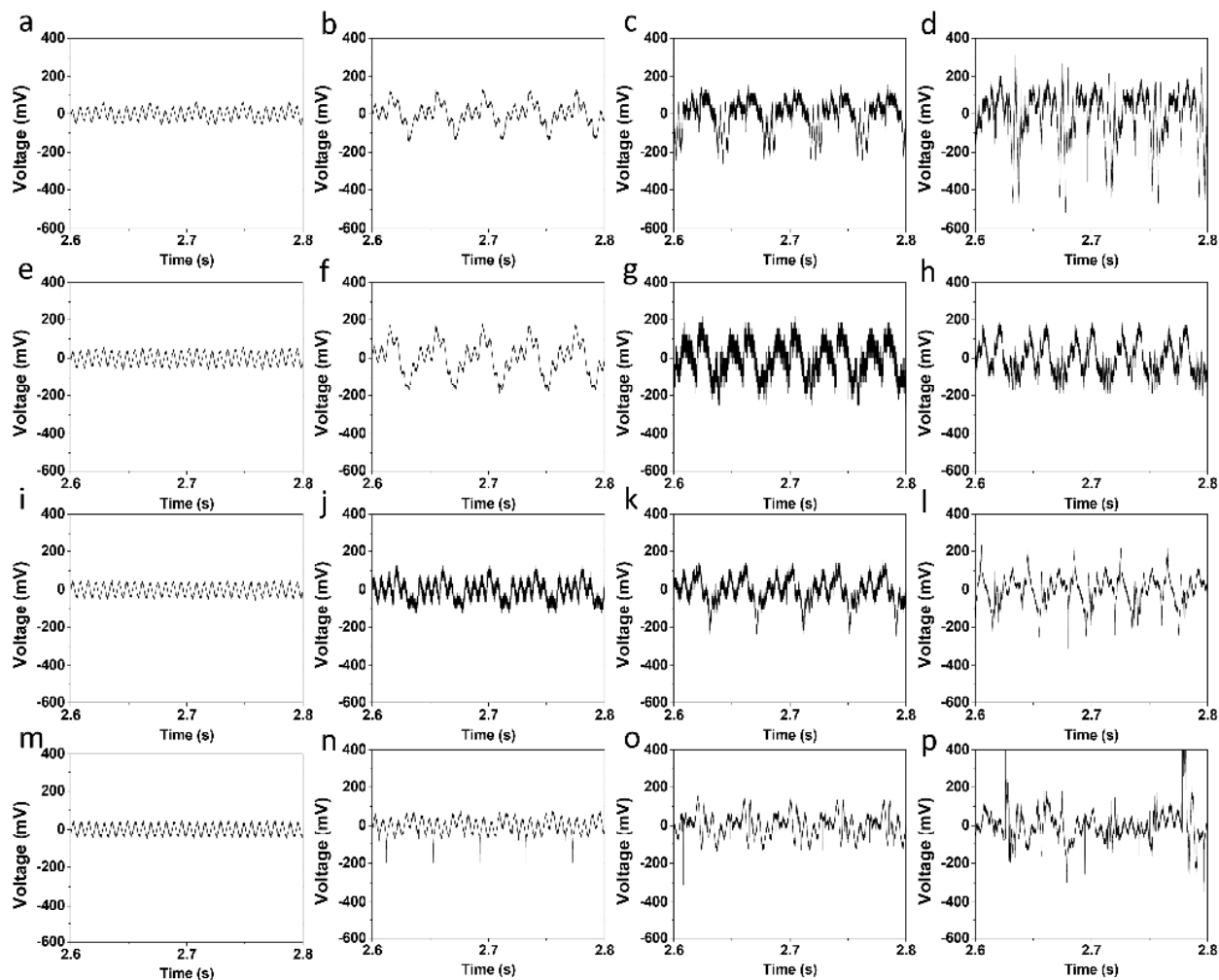
Figure S3. Representative voltage generation from electrospun P(VDF-TrFE) nanofiber mats having various average fiber diameters. Voltage output of the mats composed of average fiber diameters of 90 (a-d), 166 (e-h), 242 (i-l), and 859 nm (m-p) by surface strain of 0.03% (a,e,i,m), to 0.06% (b,f,j,n), to 0.13% (c,g,k,o), to 0.18% (d,h,l,p) at 10 Hz.
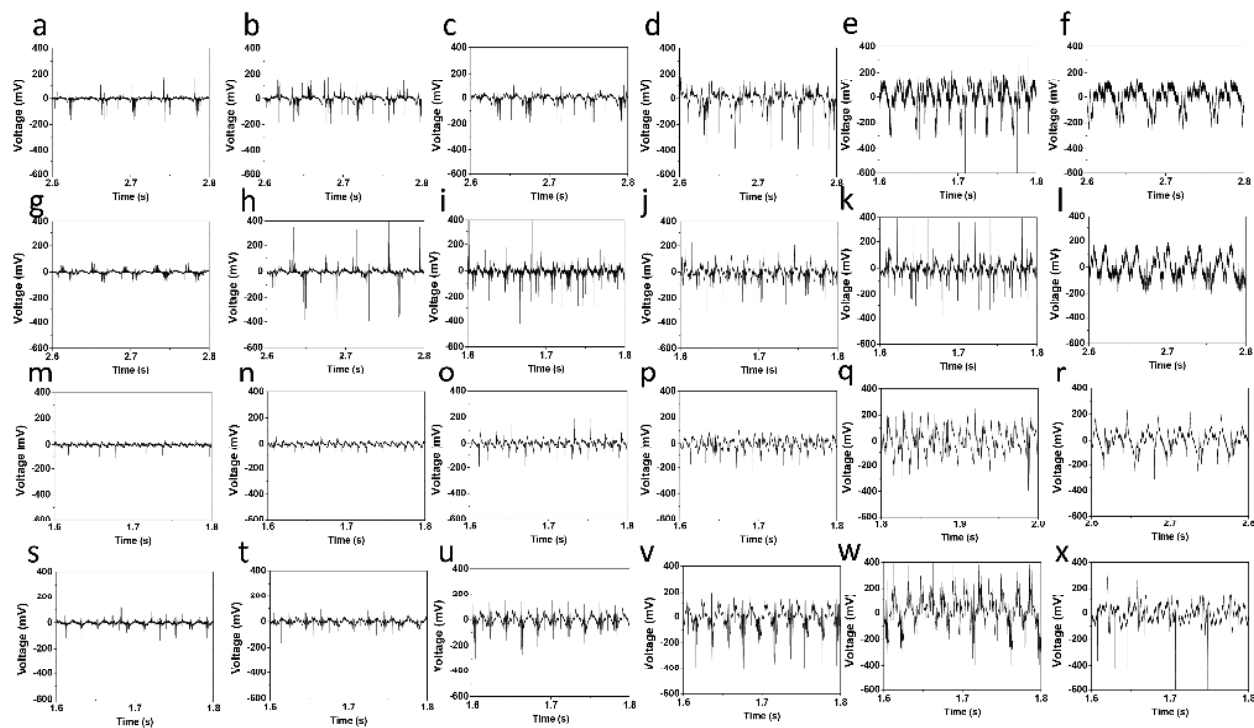
Figure S4. Representative voltage generation from electrospun P(VDF-TrFE) nanofiber mats having various average fiber diameters across varied total resistances. Voltage output of the mats composed of average fiber diameters of 90 (a-f), 166 (g-l), 242 (m-r), and 859 nm (s-x) under different total circuit resistances of 0.48 (a,g,m,s), 0.91 (b,h,n,t), 1.67 (c,i,o,u), 3.33 (d,j,p,v), 6.88 (e,k,q,w), and 10 MΩ (f,l,r,x). 0.18% of strain was applied at 10 Hz.
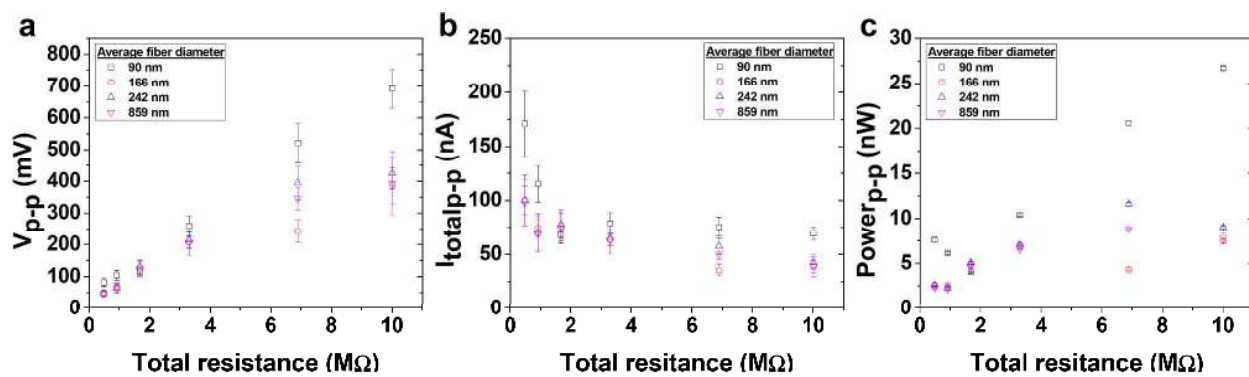
Figure S5. (a) Peak-to-peak voltage, (b) total peak-to-peak total current, and (c) peak-to-peak power of electrospun P(VDF-TrFE) nanofiber mats having various average fiber diameters. 0.18% of strain was applied at 10 Hz.
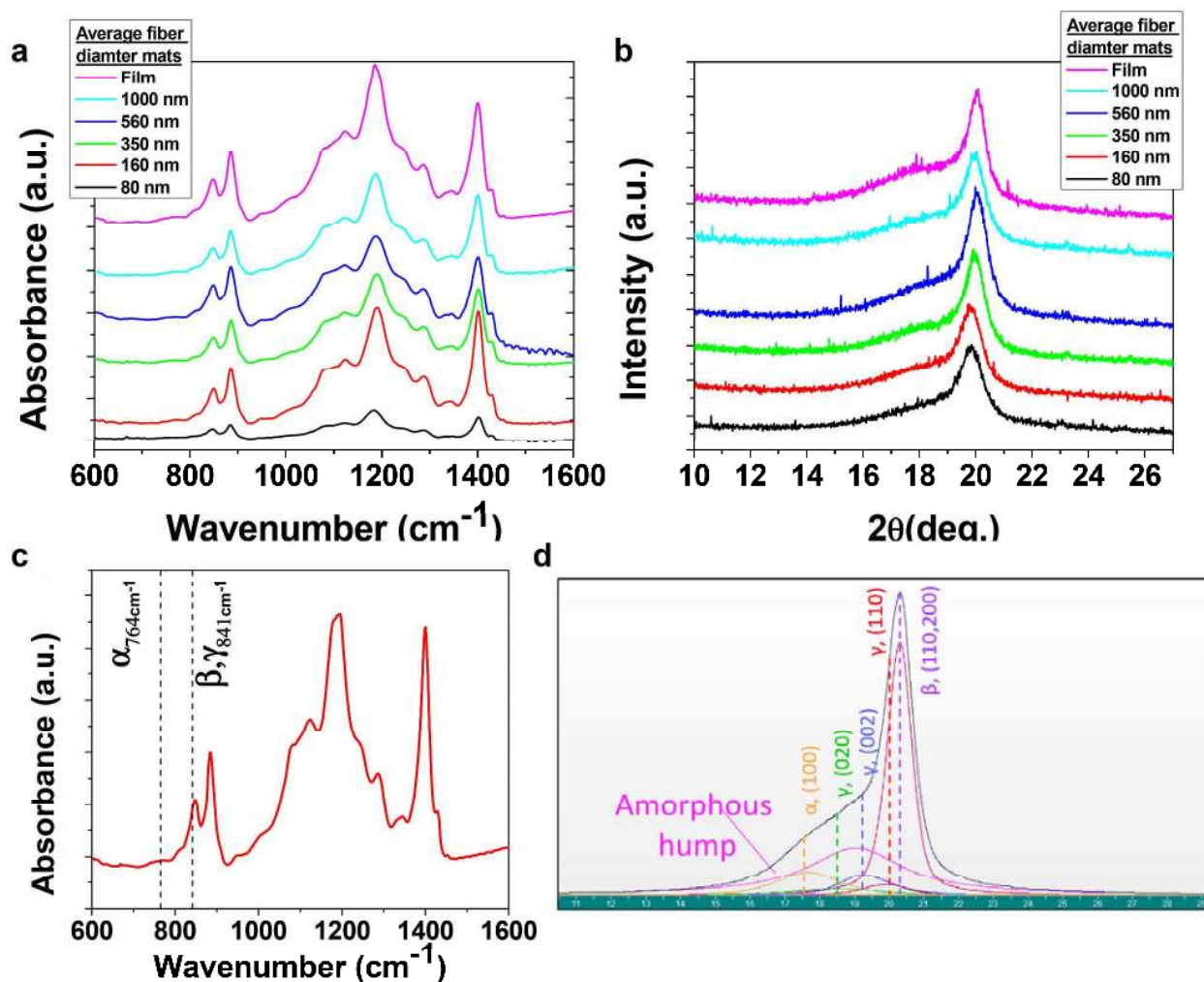
Figure S6. FTIR and XRD spectra analysis of electrospun P(VDF-TrFE) nanofibers having various fiber diameters. Representative (a) FTIR and (b) XRD spectra of electrospun P(VDF-TrFE) fibers having different average fiber diameters. Representative spectra of drop casted P(VDF-TrFE) thin film are also shown. (c) A representative FTIR spectrum with peak assignment for the α- and electroactive phases at 764 and 841 cm^{-1}, respectively. (d) An example of peak deconvolution of a representative XRD spectrum.